Coarse-graining dense, deformable active particles

Mehrana R. Nejad [1,2,*] and Julia M. Yeomans [3]
[1]Department of Physics, Harvard University, Cambridge, Massachusetts 02138, USA
[2]School of Engineering and Applied Sciences, Harvard University, Cambridge, Massachusetts 02138, USA
[3]The Rudolf Peierls Centre for Theoretical Physics, Department of Physics, University of Oxford, Parks Road, Oxford OX1 3PU, United Kingdom

(Received 20 October 2024; accepted 23 September 2025; published 17 October 2025)

We coarse-grain a model of closely packed ellipses that can vary their aspect ratio to derive continuum equations for materials comprising confluent deformable particles such as epithelial cell layers. We show that contractile nearest-neighbor interactions between ellipses can lead to their elongation and nematic ordering. Adding flows resulting from active hydrodynamic stresses produced by the particles also affects the aspect ratio and can result in active turbulence. Our results, which agree well with multiphase field simulations of deformable isotropic cells, provide a bridge between models that explicitly resolve cells and continuum theories of active matter.

DOI: 10.1103/phtt-7db6

There are many instances where the way particles can deform is important in controlling their behavior. For example, eukaryotic cells continually change shape as they move through the extracellular matrix, facilitating their motion through tight spaces [1–3]. Similarly, the shape of colloidal microgels can be controlled by temperature or humidity [4,5] and flows [6–9], which affects their response to external stimuli. Particle shape changes can also affect the collective properties of active and soft matter. Active forces result in elongation and local nematic order in epithelial monolayers, which in turn allows active turbulent flows and the creation of topological defects [10–12], and convergent extension of tissues is a common step in embryogenesis [see also Figs. 1(a) and 1(b)]. The flow properties of emulsions and foams are closely related to how they can deform under shear [13,14].

Understanding the collective behavior of deformable cells in a monolayer is a fundamental challenge in biophysics and soft matter physics. Methods that resolve individual cells, such as multiphase field and vertex models, can naturally include variations in the shape and the connectivity of individual particles. Despite the success of the approach in capturing key aspects of cellular motion and interactions, a crucial gap remains—how to systematically connect the microscopic description of deformable cells to the macroscopic continuum description. Current continuum approaches to modeling confluent cell layers and tissues rely on active nematohydrodynamics, which assumes that the shape of the constituent nematogens remains fixed [15–18]. It is not clear how to include the shape changes of individual particles in the theories of active (or passive) nematohydrodynamics, or the extent to which this will change the physics. In this work, we address this gap by performing a coarse-graining procedure that links the phase field representation of individual deformable cells to an effective continuum model that reproduces the same collective behavior. This not only improves our theoretical understanding of collective cell dynamics but also facilitates computational modeling at different scales and lays the foundation for further developments in linking deformable agent-based and continuum models. We show how shape-changing, short-range interactions can be incorporated in a manner analogous to including a Landau de Gennes free energy in fixed-particle-shape nematohydrodynamic models, and argue how to include long-range active hydrodynamic flows.

We consider a confluent system and work in terms of the coarse-grained variables $\mathbf{W}$ and $\mathcal{A}$. $\mathbf{W}$ is the anisotropy tensor, which, in two dimensions, is a 2×2 symmetric, traceless tensor that describes the coarse-grained magnitude and direction of particle *elongation*. (This is in contrast to standard nematohydrodynamics theories that consider the average *orientation* of elongated particles using a nematic tensor, $\mathcal{Q}$ [19–21].) $\mathcal{A}$ is a variable describing the locally averaged particle area.

We assume that each of the hydrodynamic variables $\mathcal{X} = \{\mathbf{W}, \mathcal{A}\}$ obeys an equation of motion of the form

$$\dot{\mathcal{X}} = \dot{\mathcal{X}}^f + \dot{\mathcal{X}}^I + \dot{\mathcal{X}}^u, \tag{1}$$

where an overdot represents a partial time derivative. $\dot{\mathcal{X}}^I$ are terms from short-range, dipolar interactions that can change particle shape. We first derive these terms, considering both forces internal to each nematogen and nearest-neighbor interactions between the particles. We then discuss $\dot{\mathcal{X}}^f$, which is similar to the fixed-particle-shape interactions that are commonly included in liquid crystal hydrodynamics as a Landau

*Contact author: mehrana@g.harvard.edu

Published by the American Physical Society under the terms of the Creative Commons Attribution 4.0 International license. Further distribution of this work must maintain attribution to the author(s) and the published article's title, journal citation, and DOI.

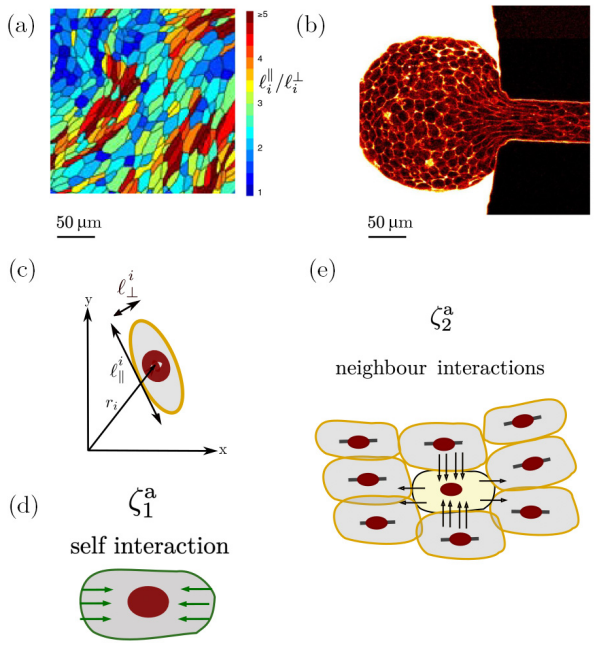


FIG. 1. (a) Activity leads to cell elongation in epithelial layers. The color code shows the aspect ratio of the cells (adapted from Ref. [22]). (b) Elongation of cells in an aggregate forced to flow through a constriction in a microfluidic channel [23]. Schematic of (c) the anisotropic Gaussian field, Eq. (2); (d) the intracellular interaction, Eq. (4); and (e) the neighbor interaction, Eq. (5).

expansion in the order parameters. We show how these contributions, along with the dipolar stresses [24], control the elongation and nematic ordering of the particles and compare the results to mesoscale simulations of confluent cell layers based on multiphase field models [25,26]. Finally, we incorporate the response of the nematogens to a flow field $\boldsymbol{u}$, $\dot{\mathcal{X}}^u$, and we discuss the active turbulence that results from a flow field driven by active hydrodynamic stresses.

I. ACTIVE SHORT-RANGE INTERACTIONS

We model individual active particles as deformable ellipses represented by Gaussian fields. The Gaussian representation is advantageous because it allows analytical progress in calculating the active particle dynamics. Particle i at position $\mathbf{r}_i$, with orientation θ_i, director $\boldsymbol{m}_i = (\cos\theta_i, \sin\theta_i)$, and long and short axes $l_i^{\parallel}$ and $l_i^{\perp}$, is described by the field

$$\varphi_i(\mathbf{r}) = e^{-(\frac{\mathbf{r}-\mathbf{r}_i}{2})\cdot(\frac{\mathbf{I}+\mathbf{q}_i}{(\ell_i^{\parallel})^2}+\frac{\mathbf{I}-\mathbf{q}_i}{(\ell_i^{\perp})^2})\cdot(\frac{\mathbf{r}-\mathbf{r}_i}{2})}, \tag{2}$$

where $\mathbf{q}_i = (2\boldsymbol{m}_i\boldsymbol{m}_i - \mathbf{I})$ is the orientation tensor with $(q_i)_{11} = -(q_i)_{22} = \cos 2\theta_i$ and $(q_i)_{12}^i = (q_i)_{21} = \sin 2\theta_i$. We note that the phase φ_i should not be interpreted as directly corresponding to a physical quantity of cell i, but rather as a useful definition that enables the study of cell-shape deformations. Figure 1(c) shows a schematic of an ellipse. We will work to linear order in the particle anisotropy and area change and derive equations of motion for the dynamics of the shape tensor:

$$\boldsymbol{d}_i = -\int d\mathbf{x}\left\{\nabla\varphi_i\nabla\varphi_i^T - \frac{\mathbf{I}}{2}\mathrm{Tr}\left(\nabla\varphi_i\nabla\varphi_i^T\right)\right\} = \frac{\pi^2}{4a_i}\mathbf{w}_i, \tag{3}$$

where we have defined cell area $a_i = \pi\ell_i^{\parallel}\ell_i^{\perp}$ and cell anisotropy tensor $\mathbf{w}_i = \{(\ell_i^{\parallel})^2 - (\ell_i^{\perp})^2\}\mathbf{q}_i$.

Guided by recent work on confluent cell layers and observation of nematic $\pm 1/2$ defects, we assume that the stresses acting on the ellipses arise from force dipoles [24], consistent with active stress in a low-Reynolds-number regime, and therefore have nematic symmetry [12,17,27–30]. We will use the terminology *active* for these forces because they are driven by biological processes in individual cells. These include the polymerization and depolymerization of actin filaments and microtubules and the activity of motor proteins that bind cytoskeletal filaments and reorganize the cytoskeletal network. Moreover, cells are connected through adherens junctions, mediated by E-cadherin proteins, and this allows cells to pull on each other by employing, for example, stress fibers formed from bundles of actin filaments [31–34].

Using the phase field introduced in Eq. (2), the internal active nematic stress for the particle i can be written as

$$\boldsymbol{\pi}_i^s = -\zeta_1^{\mathrm{a}}\mathbf{d}_i\varphi_i(\mathbf{x}), \tag{4}$$

where ζ_1^{a} is the magnitude of the intracellular stress. We consider $\zeta_1^{\mathrm{a}} < 0$ corresponding to contractile forces. In addition, to account for the interactions between the cells, we include a contractile dipolar stress, $\zeta_2^{\mathrm{a}} < 0$, which acts between ellipse i and its overlapping neighbors $j \neq i$:

$$\boldsymbol{\pi}_i^n = -\zeta_2^{\mathrm{a}}\sum_{j\neq i}\mathbf{d}_j\varphi_j(\mathbf{x}). \tag{5}$$

Intracellular and neighbor active stresses are illustrated in Figs. 1(d) and 1(e) for $\zeta_1^{\mathrm{a}} < 0$ and $\zeta_2^{\mathrm{a}} < 0$.

The active force on the ellipse i, $\mathbf{f}_i^{\mathrm{a}}(\mathbf{x}) = \nabla\cdot(\boldsymbol{\pi}_i^s + \boldsymbol{\pi}_i^n)$, then reads [25]

$$\begin{aligned}\mathbf{f}_i^{\mathrm{a}}(\mathbf{x}) &= -\zeta_1^{\mathrm{a}}\mathbf{d}_i\cdot\nabla\varphi_i(\mathbf{x}) - \zeta_2^{\mathrm{a}}\sum_{j\neq i}\mathbf{d}_j\cdot\nabla\varphi_j(\mathbf{x})\\ &\approx -\zeta_1^{\mathrm{a}}\mathbf{d}_i\cdot\nabla\varphi_i(\mathbf{x}) + \zeta_2^{\mathrm{a}}\sum_{j\neq i}\mathbf{d}_j\cdot\nabla\varphi_i(\mathbf{x}),\end{aligned} \tag{6}$$

where in the second step we have used the approximation $\nabla\varphi_j \approx -\nabla\varphi_i$, which is valid when the ellipses are close to confluent and implies that the interfaces of neighboring cells are locally parallel. In this highly packed regime, the sum of the integrals of the phases would be close to the total area of the system. Assuming overdamped dynamics and, for now, ignoring passive forces, the dynamics of the phase field is given by

$$\dot{\varphi}_i = -\frac{\mathbf{f}_i^{\mathrm{a}}}{\Gamma}\cdot\nabla\varphi_i, \tag{7}$$

where Γ is a friction coefficient. Using Eqs. (6) and (7), the Gaussian form (2) chosen for the particle shape then allows an analytic calculation of the time evolution of the anisotropy tensor (3), leading to (see Appendix A 1)

$$\dot{\mathbf{w}}_i = -(\alpha_i\mathbf{w}_i + \bar{\alpha}_i\tilde{\mathbf{w}}_i), \tag{8}$$

where $\tilde{\mathbf{w}}_i = \sum_{j\neq i}\mathbf{w}_j$, $\bar{\alpha}_i = 8\pi^2\zeta_2^{\mathrm{a}}/(27\Gamma a_i)$, and $\alpha_i = -8\pi^2\zeta_1^{\mathrm{a}}/(27\Gamma a_i)$. It is also possible to calculate the effect of the active interactions on the dynamics of the ellipse area. Noting that $a_i = \frac{1}{2}\int \varphi_i d\mathbf{x}$,

$$\dot{a}_i = \frac{1}{2}\int d\mathbf{x}\dot{\varphi}_i = -\int d\mathbf{x}\frac{\mathbf{f}_i^a}{2\Gamma}\cdot\nabla\varphi_i = c_i\mathbf{w}_i:\mathbf{w}_i + \bar{c}_i\mathbf{w}_i:\tilde{\mathbf{w}}_i, \tag{9}$$

where $c_i = -\pi^4\zeta_1^a/(32a_i^2\Gamma)$, $\bar{c}_i = \pi^4\zeta_2^a/(32a_i^2\Gamma)$, and the final step follows from Eq. (6) and the definition of the anisotropy tensor (3), and by assuming that the spatial variation of the area is slow compared to the cell anisotropy.

To introduce the active interactions into the hydrodynamic equations of the fields associated with particle shape and area, we need to rewrite Eqs. (8) and (9) in terms of coarse-grained field variables defined as

$$\mathbf{W}(\mathbf{r},t) = \langle\mathbf{w}\rangle = \int \mathbf{w}\,\psi\,da\,d\mathbf{w}\,, \tag{10}$$

$$\mathcal{A}(\mathbf{r},t) = \langle a\rangle = \int a\,\psi\,da\,d\mathbf{w}, \tag{11}$$

where $\psi(\mathbf{r},t,a,\mathbf{w})$ is the single-particle probability distribution function (see Appendix for more details). The probability density function evolves due to the particle velocity $\dot{\mathbf{r}}$, anisotropy current $\dot{\mathbf{w}}$, and area current $\dot{a}$, and its dynamics reads

$$\partial_t\psi(\mathbf{r},t,a,\mathbf{d}) = -\nabla_r\cdot(\dot{\mathbf{r}}\psi) - \nabla_a(\dot{a}\psi) - \nabla_{\mathbf{w}}:(\dot{\mathbf{w}}\psi). \tag{12}$$

We use a mean-field approximation to write the effect of the neighbors in the dynamics in Eqs. (8) and (9) as

$$\dot{\mathbf{w}}_i = -(\alpha_i\mathbf{w}_i + \bar{\alpha}_i\bar{\mathbf{W}}), \tag{13}$$

$$\dot{a}_i = c_i\mathbf{w}_i:\mathbf{w}_i + \bar{c}_i\mathbf{w}_i:\bar{\mathbf{W}}, \tag{14}$$

where $\bar{\mathbf{W}} = \mathbf{W} + \frac{r_0^2}{2}\nabla^2\mathbf{W}$, r_0 is a length scale over which neighboring ellipses interact, and we have assumed that the distribution function is isotropic in space.

Equations (10)–(14) then give the contributions of internal and neighbor active nematic interactions to the dynamics of the fields as (see Appendix A 2)

$$\dot{\mathbf{W}}^I = -\bar{\alpha}\bar{\mathbf{W}} - \alpha\mathbf{W}, \tag{15}$$

$$\dot{\mathcal{A}}^I = \bar{c}\mathbf{W}:\bar{\mathbf{W}} + \frac{c}{2}\mathbf{W}:\mathbf{W}, \tag{16}$$

where $\bar{\alpha} = 8\pi^2\zeta_2^{\mathrm{a}}/(27\Gamma\mathcal{A}_0)$, $\alpha = -8\pi^2\zeta_1^{\mathrm{a}}/(27\Gamma\mathcal{A}_0)$, $c = -\pi^4\zeta_1^a/(32\mathcal{A}_0^2\Gamma)$, and $\bar{c} = \pi^4\zeta_2^a/(32\mathcal{A}_0^2\Gamma)$.

II. PASSIVE SHORT-RANGE INTERACTIONS

We follow the standard practice of including thermodynamic interactions in the nematohydrodynamic equations for fixed-shape particles by incorporating a term $\dot{\mathcal{X}}^f = -\Gamma_{\mathcal{X}}\frac{\delta\mathcal{F}}{\delta\mathcal{X}}$, which describes relaxational dynamics to the minimum of a free energy $\mathcal{F}$ at a rate proportional to $\Gamma_{\mathcal{X}}$. The free energy is defined as a Landau expansion in the order parameters, here the anisotropy tensor $\mathbf{W}$ and the area $\mathcal{A}$:

$$\mathcal{F} = \frac{C_{\mathbf{W}}}{4}(1+\mathbf{W}:\mathbf{W})^2 + \frac{K_{\mathbf{W}}}{2}|\nabla\mathbf{W}|^2 + \frac{C_{\mathcal{A}}}{2}(\mathcal{A}-\mathcal{A}_0)^2 + \frac{C'_{\mathcal{A}}}{4}(\mathcal{A}-\mathcal{A}_0)^4 + \frac{K_{\mathcal{A}}}{2}|\nabla\mathcal{A}|^2. \tag{17}$$

In Eq. (17), the term with coefficient $C_{\mathbf{W}} > 0$ favors relaxation of the cells to an isotropic shape, and the term with the coefficient $K_{\mathbf{W}} > 0$ is an elastic free energy density that tends to align the anisotropic nematogens [29]. The terms in area $\mathcal{A}$ favor relaxation to a homogeneous area $\mathcal{A}_0$, with the gradient term penalizing inhomogeneities in area. The fourth-order terms in area and cell anisotropy are primarily included to aid numerical stability at large activities.

III. COMPETITION BETWEEN ACTIVE AND PASSIVE INTERACTIONS

We next discuss how the active and passive interactions combine to affect the shape and relative orientation of the cells. From Eqs. (15)–(17), the equations of motion for particle shape and area are

$$\dot{\mathbf{W}} = \left\{\Gamma_{\mathbf{W}}K_{\mathbf{W}} - \frac{\bar{\alpha}r_0^2}{2}\right\}\nabla^2\mathbf{W} - \{\bar{\alpha}+\alpha+\Gamma_{\mathbf{W}}C_{\mathbf{W}}(1+\mathbf{W}:\mathbf{W})\}\mathbf{W}, \tag{18}$$

$$\dot{\mathcal{A}} = -\Gamma_{\mathcal{A}}(C_{\mathcal{A}}(\mathcal{A}-\mathcal{A}_0) + C'_{\mathcal{A}}(\mathcal{A}-\mathcal{A}_0)^3 - K_{\mathcal{A}}\nabla^2\mathcal{A}) + \left(\bar{c}+\frac{c}{2}\right)\mathbf{W}:\mathbf{W} + \frac{\bar{c}r_0^2}{2}\mathbf{W}:\nabla^2\mathbf{W}. \tag{19}$$

The first term in Eq. (18) defines an effective elastic constant $\Gamma_{\mathbf{W}}K_{\mathbf{W}} - \bar{\alpha}r_0^2/2$. Note that this becomes negative for sufficiently large and positive active interactions between ellipses, destabilizing any nematic alignment and suggesting that the nematogens prefer to align perpendicular to each other. Perpendicular alignment has been observed in mesoscopic, multiphase field simulations of active deformable cell monolayers with $\bar{\alpha} > 0$ [25], and in simulations of self-propelling hard rods [35] and dividing cylindrical bacterial systems [36]. However, it means that our assumption of small deviation between neighboring nematogens used in the mean-field approximation and ignoring higher-order moments of the distribution function is not correct and therefore we have restricted ourselves to considering $\bar{\alpha} < 0$.

The second line of Eq. (18) implies a competition between active and passive terms in changing the shape of the cells. Sufficiently negative α and $\bar{\alpha}$ destabilize the isotropic shape and lead to a homogeneous steady-state solution for the elongation $|\mathbf{W}|_{\mathrm{st}}$ given by

$$|\mathbf{W}|_{\mathrm{st}}^2 = -\frac{(\bar{\alpha}+\alpha)}{\Gamma_{\mathbf{W}}C_{\mathbf{W}}} - 1. \tag{20}$$

Figure 1(e) shows schematically that contractile neighbor interactions with negative $\bar{\alpha}$ ($\zeta_2^a < 0$, black arrows) favor elongation.

The homogeneous steady-state area $\mathcal{A}_{\rm st}$ then follows from Eq. (19):

$$\mathcal{A}_{\rm st} = \mathcal{A}_0 + \frac{(\bar{c} + c/2)}{\Gamma_{\mathbf{A}} C_{\mathbf{A}}} |\mathbf{W}|_{\rm st}^2. \tag{21}$$

Equation (21) indicates that the cell area decreases with elongation ($|\mathbf{W}|_{\rm st}^2 \neq 0$) in the presence of large contractile neighbor activity. The prediction agrees with multiphase field simulations of active deformable cells [25] that show hole formation in monolayers with $\bar{c} \sim \zeta_2^a < 0$ corresponding to a decrease in cell area.

IV. LONG-RANGE FLOWS

In Appendix A 3, we show that the contribution of an imposed incompressible velocity field $\boldsymbol{u}$ to the dynamics of the anisotropy and area fields, assuming a small cell anisotropy $(\ell_i^{\parallel}/\ell_i^{\perp}) - 1$, is

$$\dot{\mathbf{W}}^u = -\boldsymbol{u} \cdot \nabla \mathbf{W} + \boldsymbol{\Omega} \cdot \mathbf{W} - \mathbf{W} \cdot \boldsymbol{\Omega} + \boldsymbol{E}, \tag{22}$$

$$\dot{\mathcal{A}}^u = -\boldsymbol{u} \cdot \nabla \mathcal{A}, \tag{23}$$

where $\boldsymbol{\Omega}$ and $\boldsymbol{E}$ are the asymmetric and symmetric parts of the velocity gradient tensor. The evolution of $\mathbf{W}$ is very similar to the dynamics of a nematic liquid crystal in an isotropic phase and with a positive flow aligning parameter $\lambda = 1$ [38]. The positive value of λ shows the tendency of the isotropic particles to extend along the largest positive eigenvector of the strain rate tensor.

As an example, we assume that the velocity field is created by the active particles themselves and that the dynamics of the incompressible fluid with density ρ and viscosity η is given by the Navier-Stokes equation,

$$\rho(\dot{\boldsymbol{u}} + \boldsymbol{u} \cdot \nabla \mathbf{u}) = \nabla P + \eta \nabla^2 \boldsymbol{u} + \zeta \nabla \cdot \mathbf{W}, \tag{24}$$

$$\nabla \cdot \boldsymbol{u} = 0, \tag{25}$$

where P is the pressure field and $\zeta \nabla \cdot \mathbf{W}$ is the usual activity term that results from coarse-graining the stresslet flow fields resulting from particle motion.

Solving Eqs. (1), (24), and (25) numerically (see Appendix A 5) results in the phase diagram and corresponding values for cell elongation and velocity gradients [shown in Figs. 2(a) and 2(b)]. Three different regions are observed. For $(\tilde{\alpha} + \alpha)/(\Gamma_W C_W) > -1$ [Eq. (20)] the cells remain isotropic and the velocity is zero unless ζ is sufficiently large and positive, when the extensional flows can elongate the particles to give a nematic state. As $(\tilde{\alpha} + \alpha)/(\Gamma_W C_W)$ decreases from -1, short-range forces between neighbors elongate the particles to give a nematic state, with hydrodynamic flows tending to enhance or suppress the elongation for $\zeta > 0$ or $\zeta < 0$, respectively. For sufficiently extended particles, there is an active instability and the nematic state becomes unstable, giving rise to active turbulence, characterized by a chaotic flow field and motile topological defects.

By coarse-graining a model of closely packed ellipses that can vary their aspect ratio, we have derived continuum equations for confluent deformable particles, an important example of which is epithelial cell layers. We show that contractile neighbor interactions, modeling the effects of actin filaments and stress fibers, compete with cell intracellular contractility and cause collective cell elongation and, when flows are permitted, form $\pm 1/2$ defects. The simplicity of the model suggests the possibility of studying how, for example, traction forces, active line tension, or different particle symmetries could be included in a continuum model of deformable particles.

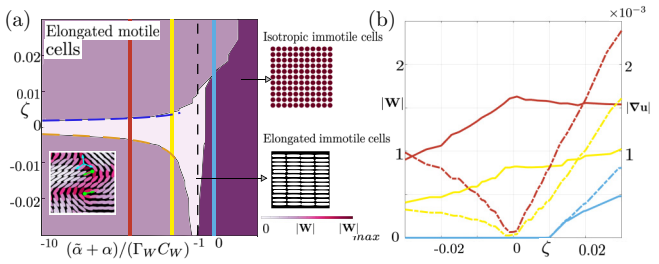


FIG. 2. (a) Phase diagram for a deformable active monolayer. The x axis describes short-range interactions [Eq. (20)] and the y axis describes the effects of stresslet-induced flows [Eq. (24)]. Three different phases are observed: a stationary isotropic phase, a stationary nematic phase, and an active phase with nonzero velocity and defect formation (active turbulence [37]). The dashed black line follows from Eq. (20) and the blue and orange dashed lines from a linear stability analysis deep in the elongated phase (see Appendix A 4). (b) Cell-shape anisotropy (solid line, left axis) and velocity gradient (dashed line, right axis) along the lines marked in panel (a). The anisotropic shape of the curves is because $\zeta > 0$ ($\zeta < 0$) facilitates (suppresses) cell elongation. The schematics show simulation results, where the aspect ratio is used to plot the ellipses.

Our results reproduce many of the features seen in multiphase field models, which resolve the boundaries of individual cells [39]. Phase field simulations show that contractile intracellular interactions result in isotropic cell shapes, whereas extensile intracellular interactions lead to cell elongation and nematic ordering [25,26]. They predict that extensile neighbor-neighbor interactions lead to a frustrated phase, where cells try to align perpendicular to their neighbors, and that contractile neighbor-neighbor interactions result in cell elongation and strong nematic ordering of neighboring cells. We observe the same trends in cell orientation, alignment, and elongation in our model, as follows from Eqs. (15) and (20). Additionally, phase field models predict that contractile neighbor-neighbor interactions ($\zeta_2 < 0$) lead to a decrease in cell area, as captured by Eq. (21) in our continuum description.

Applying mechanical pressure to airway epithelial cells leads to cell motion and an unjamming transition [22]. The mechanical compression elongates the cells and enhances collective migration without disrupting junctional integrity. This is in agreement with our results that a critical value of activity is needed for the formation of active flows and that the dynamics of the monolayer increases as cells elongate. A relation between cell deformability and collective motility has also been observed in other experiments on deformable cell

monolayers [23,31,33], as predicted for the motile phase in Fig. 2.

To further investigate active stress in cell monolayer experiments, laser ablation can be used to quantify cell-cell interactions. Furthermore, distinguishing between intracellular activity and cell-cell interactions would be of interest, which could be achieved by using traction force microscopy to measure the stress exerted by cells on a substrate, both in isolation and in contact with other cells [40].

ACKNOWLEDGMENTS

We thank Guanming Zhang, Delia Cropper, Ioannis Hadjifrangiskou, James Graham, and Sumesh Thampi for helpful discussions. J.M.Y. acknowledges support from the UK EPSRC (Award No. EP/W023849/1) and ERC Advanced Grant ActBio (funded as UKRI Frontier Research Grant No. EP/Y033981/1).

APPENDIX

1. Dynamics of the anisotropy tensor

To find the dynamics of the anisotropy tensor due to internal interactions, we first consider the time evolution of the shape tensor. From Eq. (3), this is

$$\dot{\boldsymbol{d}}_{ij} = -\int d\mathbf{x}\Big\{\nabla_i\dot{\varphi}\nabla_j\varphi + \nabla_j\dot{\varphi}\nabla_i\varphi - \frac{\delta_{ij}}{2}\partial_t((\partial_x\varphi)^2 + (\partial_y\varphi)^2)\Big\}, \tag{A1}$$

where the overdot denotes a time derivative, and we have dropped the particle subscripts, and ij label matrix elements. Hence, we need to calculate integrals of the form

$$-\int d\mathbf{x}\{\nabla_i\dot{\varphi}\nabla_j\varphi\}, \tag{A2}$$

which, using Eqs. (4) and (7), can be rewritten as

$$-\frac{d_{mn}\zeta_1^a}{\Gamma}\left\{\int d\mathbf{x}\{\nabla_i\nabla_n\varphi\nabla_m\varphi\nabla_j\varphi + \nabla_i\nabla_m\varphi\nabla_n\varphi\nabla_j\varphi\}\right\}. \tag{A3}$$

This results in numerous terms; however, the only nonzero contributions are those of the form

$$\int d\mathbf{x}\nabla_i\nabla_x\varphi\nabla_x\varphi\nabla_j\varphi = \frac{2\pi}{27\ell_\parallel\ell_\perp}\delta_{iy}\delta_{jy},$$

$$\int d\mathbf{x}\nabla_i\nabla_y\varphi\nabla_x\varphi\nabla_j\varphi = -\frac{4\pi}{27\ell_\parallel\ell_\perp}\delta_{iy}\delta_{jx} + \frac{2\pi}{27\ell_\parallel\ell_\perp}\delta_{ix}\delta_{jy},$$

$$\int d\mathbf{x}\nabla_i\nabla_x\varphi\nabla_y\varphi\nabla_j\varphi = -\frac{4\pi}{27\ell_\parallel\ell_\perp}\delta_{ix}\delta_{jy} + \frac{2\pi}{27\ell_\parallel\ell_\perp}\delta_{iy}\delta_{jx},$$

$$\int d\mathbf{x}\nabla_i\nabla_y\varphi\nabla_y\varphi\nabla_j\varphi = \frac{2\pi}{27\ell_\parallel\ell_\perp}\delta_{ix}\delta_{jx}.$$

Substituting the nonzero integrals into Eq. (A3) gives the dynamics of the shape tensor due to the self-interaction:

$$\dot{\mathbf{d}}_i = \frac{8\pi\zeta_1^a}{27\Gamma\ell_\parallel\ell_\perp}\mathbf{d}_i. \tag{A4}$$

The contribution of the neighbor interactions can be calculated using the same approach. Combining self and neighbor terms, we find

$$\dot{\mathbf{d}}_i = -(\alpha_i\mathbf{d}_i + \bar{\alpha}_i\tilde{\mathbf{d}}_i), \tag{A5}$$

where $\tilde{\mathbf{d}}_i = \sum_{j\neq i}\mathbf{d}_j$, $\bar{\alpha}_i = 8\pi^2\zeta_2^a/(27\Gamma a_i)$, $\alpha_i = -8\pi^2\zeta_1^a/(27\Gamma a_i)$, and $a_i = \pi\ell_i^\perp\ell_i^\parallel$.

Equation (3) gives the relationship between the shape tensor, the cell area, and the cell anisotropy. Assuming small cell anisotropy, and keeping terms to order $\mathbf{w}_i$, we may ignore the time dependence of the area, giving

$$\dot{\mathbf{w}}_i = -\left(\alpha_i\mathbf{w}_i + \bar{\alpha}_i a_i\sum_{j\neq i}\mathbf{w}_j/a_j\right). \tag{A6}$$

2. Dynamics of fields

To derive a coarse-grained description of the dynamics, we define the distribution function as

$$\psi(\mathbf{r},\mathbf{w},a,t) = \sum_i\psi_i(\mathbf{r},\mathbf{w},g,t), \tag{A7}$$

$$\psi_i(\mathbf{r},\mathbf{w},a,t) = \delta(\mathbf{r}-\mathbf{r}_i(t))\delta(a-a_i(t))\delta(\mathbf{w}-\mathbf{w}_i(t)). \tag{A8}$$

The dynamics of the distribution function is then

$$\begin{aligned}\partial_t\psi &= \sum_i\{\dot{\mathbf{r}}_i\cdot\nabla_{ri} + \dot{a}_i\partial_{ai} + \dot{\mathbf{w}}_i:\nabla_{\mathbf{w}i}\}\psi_i\\ &= -\nabla_r\cdot(\dot{\mathbf{r}}\psi) - \nabla_a(\dot{a}\psi) - \nabla_{\mathbf{w}}(\dot{\mathbf{w}}\psi).\end{aligned} \tag{A9}$$

We assume that the cells in the monolayer do not self-propel and only move with the average flow. As a result, we set $\dot{\mathbf{r}} = 0$, and we study the effect of the flows in Appendix A 3. Using Eqs. (13) and (14), we find the dynamics of the distribution function

$$\begin{aligned}\partial_t\psi =& -\partial_a((c\mathbf{w}:\mathbf{w} + \bar{c}\mathbf{w}:\tilde{\mathbf{W}})\psi)\\ &+ \nabla_{\mathbf{w}}:((\alpha\mathbf{w} + \bar{\alpha}\tilde{\mathbf{W}}\psi)).\end{aligned} \tag{A10}$$

We then use the evolution of the distribution function [Eq. (A10)] and the definition of the area field [Eq. (11)] to find the dynamics of the area field. This is straightforward for the neighbor interaction [term with coefficient $\bar{c}$ in Eq. (A10)] as $\mathbf{w}$ only appears to first order here. The contribution from self-interaction (term with coefficient c), however, is second order in $\mathbf{w}$ and we need to introduce a closure scheme to be able to proceed with the calculations. Since we are interested in a system where cells are isotropic in the absence of activity, we choose a closure scheme in which traceless moments higher than $\mathbf{w}$ go to zero. In particular, assuming that the fourth-order moment,

$$\begin{aligned}T_{ijkl} =& m_im_jm_km_l - \tfrac{1}{6}[\delta_{ij}m_km_l + \delta_{ik}m_jm_l + \delta_{il}m_km_j\\ &+ \delta_{lj}m_km_i + \delta_{kj}m_im_l + \delta_{kl}m_im_j]\\ &+ \tfrac{1}{24}[\delta_{kl}\delta_{ij} + \delta_{kj}\delta_{il} + \delta_{ki}\delta_{lj}],\end{aligned} \tag{A11}$$

is negligible, we can find the contribution from the self-interaction to the dynamics of the area field. A straightforward but lengthy calculation gives

$$\dot{\mathcal{A}} = \frac{c}{2}\mathbf{W}:\mathbf{W} + \bar{c}\mathbf{W}:\tilde{\mathbf{W}}. \tag{A12}$$

Finally, it is straightforward to find the dynamics of the anisotropy field as $\mathbf{w}$ only appears in the first order (terms with coefficients α and $\bar{\alpha}$). The resulting equation is

$$\dot{\mathbf{W}} = -(\alpha \mathbf{W} + \bar{\alpha}\tilde{\mathbf{W}}). \tag{A13}$$

3. Effect of flow

To find the dynamics of the cell anisotropy, we need to calculate integrals of the form

$$(\mathcal{J}_i)_{mn} = -\int d\mathbf{x}\{\nabla_n \varphi_i \nabla_m \dot{\varphi}_i\}. \tag{A14}$$

We assume that the velocity field changes the phase field φ_i according to $\dot{\varphi}_i = -\mathbf{u}\cdot\nabla\varphi_i$. Therefore,

$$\nabla_m \dot{\varphi}_i = -\nabla_m(\mathbf{v}\cdot\nabla\varphi_i) = -\nabla_m v_p \nabla_p \varphi_i - v_p \nabla_p \nabla_m \varphi_i. \tag{A15}$$

In addition, we assume that the velocity field changes slowly on the scale of the particles, and take the velocity terms out of the integral. Using this approximation, $(\mathcal{J}_i)_{mn}$ can be written as

$$(\mathcal{J}_i)_{mn} \approx \nabla_m u_p \int d\mathbf{x} \nabla_n \varphi_i \nabla_p \varphi_i + u_p \nabla_p \int d\mathbf{x} \nabla_n \varphi_i \nabla_m \varphi_i. \tag{A16}$$

Calculating the integrals then enables us to find the dynamics of the anisotropy tensor as

$$\dot{\mathbf{w}}_i = -\boldsymbol{u}\cdot\nabla\mathbf{w}_i + \frac{(1+[\epsilon_i+1]^2)}{2\epsilon_i+2}\mathbf{E} + \boldsymbol{\Omega}\cdot\mathbf{w}_i - \mathbf{w}_i\cdot\boldsymbol{\Omega}, \tag{A17}$$

where $\epsilon_i = (\ell_i^{\parallel}/\ell_i^{\perp}) - 1$ is the eccentricity of the cell. Consecutive terms on the right-hand side of Eq. (A17) show the advection of the particle by the flow field, the effect of the strain rate, $\mathbf{E} = (\nabla\boldsymbol{u}^T + \nabla\boldsymbol{u})/2$, on the change in the shape of the particle, and the effect of vorticity, $\boldsymbol{\Omega} = (\nabla\boldsymbol{u}^T - \nabla\boldsymbol{u})/2$, on the particle orientation. Assuming a small particle anisotropy $\epsilon_i = \ell_{\parallel}^i/\ell_{\perp}^i - 1$ and keeping the leading order term in the eccentricity $[\mathcal{O}(\epsilon_i^0)]$, Eq. (A17) simplifies to

$$\dot{\mathbf{w}}_i = -\boldsymbol{u}\cdot\nabla\mathbf{w}_i + \mathbf{E} + \boldsymbol{\Omega}\cdot\mathbf{w}_i - \mathbf{w}_i\cdot\boldsymbol{\Omega}. \tag{A18}$$

Using Eqs. (A9) and (A18), we then arrive at Eq. (22) for the dynamics of the anisotropy field. The dynamics of the cell area due to the flows can be easily calculated using the dynamics of the phase field (7) as

$$\dot{a}_i \approx -\frac{\mathbf{u}}{2}\cdot\nabla\int d\mathbf{x}\varphi_i. \tag{A19}$$

Using Eqs. (A9) and (A19) gives the dynamics of the area field [Eq. (23)],

$$\dot{\mathcal{A}}^u = -\boldsymbol{u}\cdot\nabla\mathcal{A}. \tag{A20}$$

4. Linear stability analysis

In Appendix A 3 we compare the results of the numerical simulations (shown in Fig. 2) with the linear stability analysis. We analyze the growth rate of perturbations in the fields, given by $\mathcal{R} = \mathcal{R}^0 + \delta\tilde{R}$, where $\mathcal{R}^0$ represents the steady-state solution and $\delta\tilde{R}(\mathbf{r},t) = \int \delta\mathcal{R}e^{i\mathbf{q}\cdot\mathbf{r}+\omega t}d\mathbf{q}d\omega$ denotes the perturbation around the steady state, deep in the anisotropic phase. Using Eqs. (1), (24), and (25), along with the steady-state solutions $\mathbf{u}^0 = 0$, $W_{ij}^0 = |\mathbf{W}|_{\rm st}\delta_{i1}\delta_{j1}$, we find that the perturbations in $\delta\tilde{W}_{xx}$ decay, while the growth rate of the perturbations in $\delta\tilde{W}_{xy}$ is given by

$$\omega = \frac{-4\Gamma_{\mathbf{W}}K_{\mathbf{W}}q^2\eta + 2\bar{\alpha}q^2r_0^2\eta + 3\zeta + 4\zeta|\mathbf{W}|_{\rm st}\cos(2\theta)}{4\eta} - \frac{\zeta\cos(4\theta)}{4\eta}. \tag{A21}$$

We can then determine the critical activity at which the growth rate becomes zero ($\omega = 0$):

$$\zeta_c = \frac{2\eta q^2(\bar{\alpha}r_0^2 - 2\Gamma_{\mathbf{W}}K_{\mathbf{W}})}{(\cos 4\theta - 3) - 4|\mathbf{W}|_{\rm st}\cos 2\theta}. \tag{A22}$$

We then use the parameters from the simulations and consider values of $|\mathbf{W}|_{\rm st} \geqslant 1$, which correspond to the deep anisotropic phase. We choose the angle θ between the wave vector and the direction of order that leads to the smallest needed activity to see the instability. The only remaining unknown is q, which is inversely proportional to system size, and we treat it as a fitting parameter to match the solution in Eq. (A22) with the instability boundary for $\zeta < 0$ in Fig. 2 (orange dashed line). Using this fitting parameter, the instability boundary for $\zeta > 0$ then matches with the boundary found numerically as well (blue dashed line in Fig. 2). Note that since the results of the linear stability analysis are only valid deep in the anisotropic phase, the comparison has been performed for $|\mathbf{W}|_{\rm st} = \left(-\frac{(\bar{\alpha}+\alpha)}{\Gamma_{\mathbf{W}}C_{\mathbf{W}}} - 1\right)^{1/2} \geqslant 1$.

5. Simulation methods and parameters

To plot the phase diagram in Fig. 2, we solved coupled equations (1), (24), and (25) using a hybrid lattice Boltzmann and finite difference method [41–43] with discretization length scales $\Delta x = \Delta y = 1$ and discretization timescale $\Delta t = 1$ on a 150×150, lattice over a total time of $t = 200\,000\Delta t$. In the Navier-Stokes equation, we ignored the effect of backflow and focused on the role of the active flows. We used $\Gamma = 0.4$, $C_{\mathbf{W}} = 0.001$, $-0.03 < \zeta < 0.03$, $K_{\mathbf{W}} = 0.01$, $\rho = 40$, $r_0 = 1$, $0.001 < \bar{\alpha} < 0.011$, and $-0.01 < \alpha < -0.001$.

The initial condition in all the simulations is a quiescent phase $\mathbf{u} = 0$, with circular cells with a random uniform noise in the interval $[0, 10^{-5}]$ in cell anisotropy and with an

orientation in the interval $[0, 2\pi]$. We identified the boundary points with the criteria $0 < |\nabla u| < 2.5\times10^{-4}$ and $0.1 < W < 0.12$.

6. Free energy

The free energy of the phase field model reads

$$\mathcal{F} = \mathcal{F}_{\rm CH} + \mathcal{F}_{\rm area} + \mathcal{F}_{\rm rep},$$

where the first term,

$$\mathcal{F}_{\rm CH} = \sum_i \frac{\gamma}{\lambda} \int d\mathbf{x}[4\varphi_i(\mathbf{x})^2(1-\varphi_i(\mathbf{x}))^2 + \lambda^2(\nabla\varphi_i(\mathbf{x}))^2], \tag{A23}$$

corresponds to the Cahn-Hilliard free energy, which drives φ_i toward the values 1 (inside the cell) or 0 (outside the cell) and lead to minimal cell surface area (surface tension). The second term in the free energy imposes a soft constraint on the cell area and penalizes deviations from the preferred cell area

$$\mathcal{F}_{\rm area} = \sum_i \mu\left(1 - \frac{1}{\pi R^2}\int d\mathbf{x}\ \varphi_i(\mathbf{x})^2\right)^2. \tag{A24}$$

The passive contributions to cell-cell interactions are introduced through the repulsion free energy

$$\mathcal{F}_{\rm rep} = \sum_i \sum_{j\neq i} \frac{\kappa}{\lambda} \int d\mathbf{x}\ \varphi_i(\mathbf{x})^2\varphi_j(\mathbf{x})^2, \tag{A25}$$

which penalizes the overlap between neighboring cells. Using the cell phase field in the Cahn-Hilliard free energy $\mathcal{F}_{\rm CH}$ and performing the spatial integrals yields a term that penalizes deviations of the cell shape from a circular shape, similar to the first term in the free energy in Eq. (17). The integral over the area term in the free energy produces a term similar to the third term in Eq. (17).

To determine the free energy contribution due to the repulsive interaction between cells—while excluding nonphysical spurious torques—we assume that the variables related to cell j (which is in close proximity to cell i) are similar to those associated with cell i. Expanding these in a Taylor series around cell i, and considering small cell anisotropy $\ell_\parallel^j/\ell_\perp^j \approx 1$, while retaining terms up to second order and neglecting couplings between different fields, results in the second and last terms in Eq. (17).

[1] D. A. Fletcher and R. D. Mullins, Cell mechanics and the cytoskeleton, Nature (London) **463**, 485 (2010).

[2] B. Geiger, J. P. Spatz, and A. D. Bershadsky, Environmental sensing through focal adhesions, Nat. Rev. Mol. Cell Biol. **10**, 21 (2009).

[3] L. Happel, O. Griseldis, V. Grudtsyna, H. P. Jain, R. Sknepnek, A. Doostmohammadi, and A. Voigt, Quantifying the shape of cells—from minkowski tensors to *p*-atic order, bioRxiv, 10.1101/2025.01.03.631196.

[4] B. H. Tan and K. C. Tam, Review on the dynamics and micro-structure of pH-responsive nano-colloidal systems, Adv. Colloid Interface Sci. **136**, 25 (2008).

[5] K. S. Lefroy, B. S. Murray, and M. E. Ries, Advances in the use of microgels as emulsion stabilisers and as a strategy for cellulose functionalisation, Cellulose **28**, 647 (2021).

[6] C. Misbah, Vacillating breathing and tumbling of vesicles under shear flow, Phys. Rev. Lett. **96**, 028104 (2006).

[7] J. Dupire, M. Socol, and A. Viallat, Full dynamics of a red blood cell in shear flow, Proc. Natl. Acad. Sci. USA **109**, 20808 (2012).

[8] M. Abkarian, M. Faivre, and A. Viallat, Swinging of red blood cells under shear flow, Phys. Rev. Lett. **98**, 188302 (2007).

[9] G. Kabacaoğlu and E. Lushi, Cross-stream migration of a vesicle in vortical flows, Phys. Rev. E **107**, 044608 (2023).

[10] L. Atia, D. Bi, Y. Sharma, J. A. Mitchel, B. Gweon, S. A. Koehler, S. J. DeCamp, B. Lan, J. H. Kim, R. Hirsch *et al.*, Geometric constraints during epithelial jamming, Nat. Phys. **14**, 613 (2018).

[11] A. Boromand, A. Signoriello, F. Ye, C. S. O'Hern, and M. D. Shattuck, Jamming of deformable polygons, Phys. Rev. Lett. **121**, 248003 (2018).

[12] M. R. Nejad, L. J. Ruske, M. McCord, J. Zhang, G. Zhang, J. Notbohm, and J. M. Yeomans, Stress-shape misalignment in confluent cell layers, Nat. Commun. **15**, 3628 (2024).

[13] I. Cantat, S. Cohen-Addad, F. Elias, F. Graner, R. Höhler, O. Pitois, F. Rouyer, and A. Saint-Jalmes, *Foams: Structure and Dynamics* (Oxford University Press, Oxford, 2013).

[14] D. Exerowa, G. Gochev, D. Platikanov, L. Liggieri, and R. Miller, *Foam Films and Foams: Fundamentals and Applications* (CRC Press, Cambridge, MA, 2018).

[15] D.-Q. Zhang, P.-C. Chen, Z.-Y. Li, R. Zhang, and B. Li, Topological defect-mediated morphodynamics of active–active interfaces, Proc. Natl. Acad. Sci. USA **119**, e2122494119 (2022).

[16] V. Yashunsky, D. J. G. Pearce, C. Blanch-Mercader, F. Ascione, P. Silberzan, and L. Giomi, Chiral edge current in nematic cell monolayers, Phys. Rev. X **12**, 041017 (2022).

[17] T. B. Saw, A. Doostmohammadi, V. Nier, L. Kocgozlu, S. Thampi, Y. Toyama, P. Marcq, C. T. Lim, J. M. Yeomans, and B. Ladoux, Topological defects in epithelia govern cell death and extrusion, Nature (London) **544**, 212 (2017).

[18] F. Ascione, S. Caserta, S. Esposito, V. R. Villella, L. Maiuri, M. R. Nejad, A. Doostmohammadi, J. M. Yeomans, and S. Guido, Collective rotational motion of freely-expanding T84 epithelial cell colonies, J. R. Soc. Interface **20**, 20220719 (2023).

[19] G. Duclos, C. Blanch-Mercader, V. Yashunsky, G. Salbreux, J.-F. Joanny, J. Prost, and P. Silberzan, Spontaneous shear flow in confined cellular nematics, Nat. Phys. **14**, 728 (2018).

[20] I. Lavi, R. Alert, J.-F. Joanny, and J. Casademunt, Nonlinear spontaneous flow instability in active nematics, Phys. Rev. Lett. **134**, 238301 (2025).

[21] S. Santhosh, M. R. Nejad, A. Doostmohammadi, J. M. Yeomans, and S. P. Thampi, Activity induced nematic order in isotropic liquid crystals, J. Stat. Phys. **180**, 699 (2020).

[22] J. A. Mitchel, A. Das, M. J. O'Sullivan, I. T. Stancil, S. J. DeCamp, S. Koehler, O. H. Ocaña, J. P. Butler, J. J. Fredberg, M. A. Nieto, D. Bi, and J.-A. Park, In primary airway epithelial

cells, the unjamming transition is distinct from the epithelial-to-mesenchymal transition, Nat. Commun. **11**, 5053 (2020).

[23] S. L. Tlili, F. Graner, and H. Delanoë-Ayari, A microfluidic platform to investigate the role of mechanical constraints on tissue reorganization, Development **149**, dev200774 (2022).

[24] Y. Hatwalne, S. Ramaswamy, M. Rao, and R. A. Simha, Rheology of active-particle suspensions, Phys. Rev. Lett. **92**, 118101 (2004).

[25] G. Zhang and J. M. Yeomans, Active forces in confluent cell monolayers, Phys. Rev. Lett. **130**, 038202 (2023).

[26] M. Chiang, A. Hopkins, B. Loewe, M. C. Marchetti, and D. Marenduzzo, Intercellular friction and motility drive orientational order in cell monolayers, Proc. Natl. Acad. Sci. USA **121**, e2319310121 (2024).

[27] J.-M. Armengol-Collado, L. N. Carenza, and L. Giomi, Hydrodynamics and multiscale order in confluent epithelia, elife **13**, e86400 (2024).

[28] J. M. Yeomans, S. Bhattacharyya, and M. R. Nejad, Active nematics: A new approach to mechanobiology? Liq. Cryst. 1 (2025).

[29] M. Bruna, S. J. Chapman, and M. Schmidtchen, Derivation of a macroscopic model for Brownian hard needles, Proc. R. Soc. A **479**, 20230076 (2023).

[30] M. Nejad, J. M. Yeomans, and S. P. Thampi, Cellular dynamics emerging from turbulent flows steered by active filaments, arXiv:2501.05971.

[31] J. Eckert, B. Ladoux, R.-M. Mège, L. Giomi, and T. Schmidt, Hexanematic crossover in epithelial monolayers depends on cell adhesion and cell density, Nat. Commun. **14**, 5762 (2023).

[32] L. Balasubramaniam, A. Doostmohammadi, T. B. Saw, G. H. N. S. Narayana, R. Mueller, T. Dang, M. Thomas, S. Gupta, S. Sonam, A. S. Yap *et al.*, Investigating the nature of active forces in tissues reveals how contractile cells can form extensile monolayers, Nat. Mater. **20**, 1156 (2021).

[33] D. Choi, Z. Gonzalez, S. Y. Ho, A. Bermudez, and N. Y. Lin, Cell-cell adhesion impacts epithelia response to substrate stiffness: Morphology and gene expression, Biophys. J. **121**, 336 (2022).

[34] A. J. Haas, C. Zihni, S. M. Krug, R. Maraspini, T. Otani, M. Furuse, A. Honigmann, M. S. Balda, and K. Matter, ZO-1 guides tight junction assembly and epithelial morphogenesis via cytoskeletal tension-dependent and-independent functions, Cells **11**, 3775 (2022).

[35] S. R. McCandlish, A. Baskaran, and M. F. Hagan, Spontaneous segregation of self-propelled particles with different motilities, Soft Matter **8**, 2527 (2012).

[36] D. Volfson, S. Cookson, J. Hasty, and L. S. Tsimring, Biomechanical ordering of dense cell populations, Proc. Natl. Acad. Sci. USA **105**, 15346 (2008).

[37] A. Doostmohammadi, J. Ignes-Mullol, J. M. Yeomans, and F. Sagués, Active nematics, Nat. Commun. **9**, 3246 (2018).

[38] M. R. Nejad and J. M. Yeomans, Spontaneous rotation of active droplets in two and three dimensions, PRX Life **1**, 023008 (2023).

[39] R. Alert and X. Trepat, Physical models of collective cell migration, Annu. Rev. Condens. Matter Phys. **11**, 77 (2020).

[40] M. Lekka, K. Gnanachandran, A. Kubiak, T. Zielinski, and J. Zemla, Traction force microscopy—Measuring the forces exerted by cells, Micron **150**, 103138 (2021).

[41] D. Marenduzzo, E. Orlandini, M. E. Cates, and J. M. Yeomans, Steady-state hydrodynamic instabilities of active liquid crystals: Hybrid lattice Boltzmann simulations, Phys. Rev. E **76**, 031921 (2007).

[42] M. R. Nejad, A. Doostmohammadi, and J. M. Yeomans, Memory effects, arches and polar defect ordering at the cross-over from wet to dry active nematics, Soft Matter **17**, 2500 (2021).

[43] F. Mackay, J. Toner, A. Morozov, and D. Marenduzzo, Darcy's law without friction in active nematic rheology, Phys. Rev. Lett. **124**, 187801 (2020).